HIGHER ORDER DISCRETIZATION MODEL FOR CODED APERTURE SPECTRAL IMAGING SYSTEMS

by

Hoover F. Rueda-Chacon

A thesis submitted to the Faculty of the University of Delaware in partial fulfillment of the requirements for the degree of Master of Science in Electrical and Computer Engineering

Spring 2015

HIGHER ORDER DISCRETIZATION MODEL FOR CODED APERTURE SPECTRAL IMAGING SYSTEMS

by

Hoover F. Rueda-Chacon

Approved: ______________________________
Gonzalo R. Arce, Ph.D.
Professor in charge of thesis on behalf of the Advisory Committee

Approved: ______________________________
Kenneth E. Barner, Ph.D.
Chair of the Department of Electrical and Computer Engineering

Approved: ______________________________
Babatunde Ogunnaike, Ph.D.
Dean of the College of Engineering

Approved: ______________________________
James G. Richards, Ph.D.
Vice Provost for Graduate and Professional Education

TABLE OF CONTENTS

LIST OF TABLES

LIST OF FIGURES

ABSTRACT

Coded Aperture Snapshot Spectral Imaging Systems (CASSI) sense the 3D spatio-spectral information of a scene using a single 2-dimensional focal plane array (FPA) snapshot. The compressive CASSI measurements are often modeled as the summation of coded and shifted versions of the spectral voxels of the underlying scene. This coarse approximation of the analog CASSI sensing phenomena is then compensated by calibration preprocessing prior to signal reconstruction. This thesis develops a higher order precision model for the optical sensing in CASSI that includes a more accurate discretization of the underlying signals, leading to image reconstructions less dependent on calibration. Further, the higher order model results in improved image quality reconstruction of the underlying scene than that achieved by the traditional model. The proposed higher precision computational model is also more suitable for reconfigurable multi-frame CASSI systems where multiple coded apertures are used sequentially to capture the hyperspectral scene. Several simulations and experimental measurements demonstrate the benefits of the new discretization model.

Chapter 1

INTRODUCTION

Spectral imaging (SI) techniques sense the two-dimensional (x, y) spatial information across a range of spectral wavelengths (λ) of a scene. Knowledge of the spectral content at various spatial locations from a scene can be valuable in identifying the composition and structure of objects of interest in the scene. SI has therefore been widely used in areas such as remote sensing [2], artwork conservation [3], and biomedical imaging [4]. Conventional SI sensors use temporal scanning either spectrally or spatially and merge the results to construct a spatio-spectral datacube [5]. These techniques are suitable for static scenes, however, it complicates and limits subsequent image processing and analysis of dynamic scenes due to the artifacts induced by the overlapping of the scanning operation. Their principal disadvantage is that they require scanning a number of regions that grows linearly in proportion to the desired spatial or spectral resolution. In contrast, compressive spectral imaging (CSI) techniques [6], first capture 2D coded projections of the underlying scene, and then, it recovers an estimate of the 3D datacube exploiting the fact that spectral images are highly correlated and admit sparse representations.

Coded Aperture Snapshot Spectral Imaging (CASSI) depicted in Fig. 1.1 is an imaging architecture that effectively senses the three dimensional (3D) spectral information of a scene, using a single 2D coded random projection measurement [1]. For spectrally rich or very detailed spatial scenes, a single shot CASSI measurement may not provide a sufficient number of compressive measurements [7, 8]. Increasing the number of measurement shots, each with a distinct coded aperture that remains fixed during the integration time of the detector, will rapidly increase the quality of image reconstruction [9, 10, 11]. Each CASSI measurement shot adds simultaneously $(N + L - 1)N$ compressive measurements. Thus, the total number of available measurements with K shots is

$m = K(N+L-1)N$. The time-varying coded apertures can be realized by a piezo system [12]. A more versatile system was developed in [13] which uses a digital micro-mirror device (DMD) to vary the random pattern in each snapshot. Given a set of focal plane array (FPA) compressive measurements, compressive sensing (CS) theory is then exploited to recover the underlying 3D spectral data cube by finding the sparsest approximation with the minimum Euclidean distance to the 2D random projection measurements. Typically, the discretized output at the CASSI detector g_{mn} is modeled as the sum of the underlying spectral voxel slices which have been previously modulated by a coded aperture and subsequently spatially dispersed by a prism. More specifically, the two dimensional CASSI output has been traditionally modeled as

$$g_{mn} = \sum_{k=0}^{L-1} f_{(m-k)jk} T_{(m-k)j}, \tag{1.1}$$

where f_{ijk} is the discretization of the underlying spatio-spectral power source density and T_{ij} is the discretized coded aperture. Notice that f_{ijk} in (1.1) is assumed to be a cubic voxel which impinges on a single pixel detector element g_{mn}. The analog sensing phenomena, however, is such that when a single voxel of a scene is dispersed by the prism, it impinges on several detector elements at a time. This, in turn, causes blurring which deteriorates the quality of image reconstruction. To ameliorate this problem, instead of

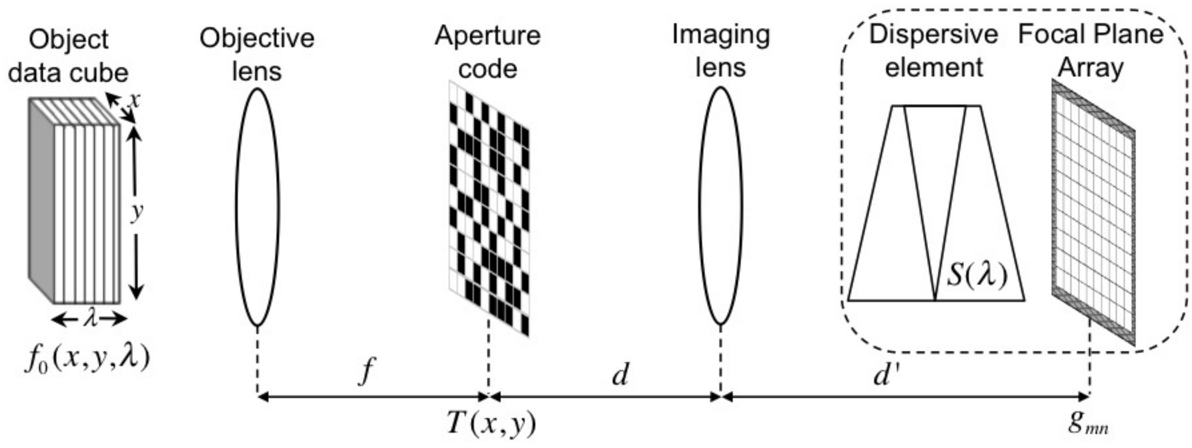

Figure 1.1: Optical elements present in CASSI.

using the coded aperture T_{ij}, a set of calibrated coded apertures $\{T_{ij}^k\}_{k=0}^{L-1}$ are experimentally measured and used in the reconstruction process to take into account the non-ideal optical blur and non-linear dispersion [14]. Thus, the model in Eq. (1.1) suffers of a coarse approximation which is then partially rectified by the coded aperture calibration process.

There are two drawbacks in this approach. First the calibration process is often inadequate such that the discretized voxels f_{ijk} are incorrectly weighted by the calibrated codes T_{ij}^k. The calibration errors originate principally from the assumption that a coded cubic voxel impinges on the detector when actually it is a coded oblique voxel which impinges on it. Secondly, calibration of the coded apertures is difficult for multiframe CASSI systems where a sequence of coded apertures are used sequentially. This work examines the sensing phenomena and determines a more precise computational model than that in Eq. (1.1). The gains include less reliance of calibration procedures in the reconstruction, as well as higher quality of image reconstruction. The higher-order model is tested through extensive simulations and experimentally in a CASSI multi-frame testbed.

Chapter 2

CODED APERTURE SNAPSHOT SPECTRAL IMAGING (CASSI)

2.1 CASSI System Description

Compressive coded aperture spectral imagers, also known as coded aperture snapshot spectral imagers (CASSI) [1, 6, 13] comprise the new generation of spectral imagers. These naturally embody the principles of compressive sensing (CS) [15, 16, 17]. The remarkable advantage of CASSI imagers is that the entire data cube is sensed with just a few FPA measurements and in some cases with as little as a single FPA shot. The CASSI instrument developed in [1] is shown in Fig. 2.1. The sensing physical phenomena in CASSI is strikingly simple, yet it adheres to the incoherence principles required in CS. CASSI measurements are realized optically by a coded aperture, a dispersive element such as a prism, and a CCD detector. The coding is applied to the spatio-spectral image source density by means of a coded aperture. The resulting coded field is subsequently modified by a dispersive element before it impinges onto the FPA detector. The compressive measurements across the FPA are realized by the integration of the coded and dispersed field.

The sensing mechanism is illustrated by the discretized model shown in Fig. 2.2, where the spectral data cube having L spectral bands and $M \times N$ spatial pixels is first amplitude modulated by a pixelated $M \times N$ coded aperture. In this case, the coded aperture is a black-and-white coded aperture such that the energy along an entire row of the data cube is "punched out" when a "black" coded aperture element is encountered. As the coded field transverses the prism, it is then spatially sheared along one spatial axis. In essence, each coded image plane is shifted along the x-axis where the amount of shifting increases with the wavelength coordinate index. Finally, the coded and dispersed field is "collapsed" in the spectral dimension by the integration of the energy impinging on each detector element over its spectral range sensitivity. The integrated field is then

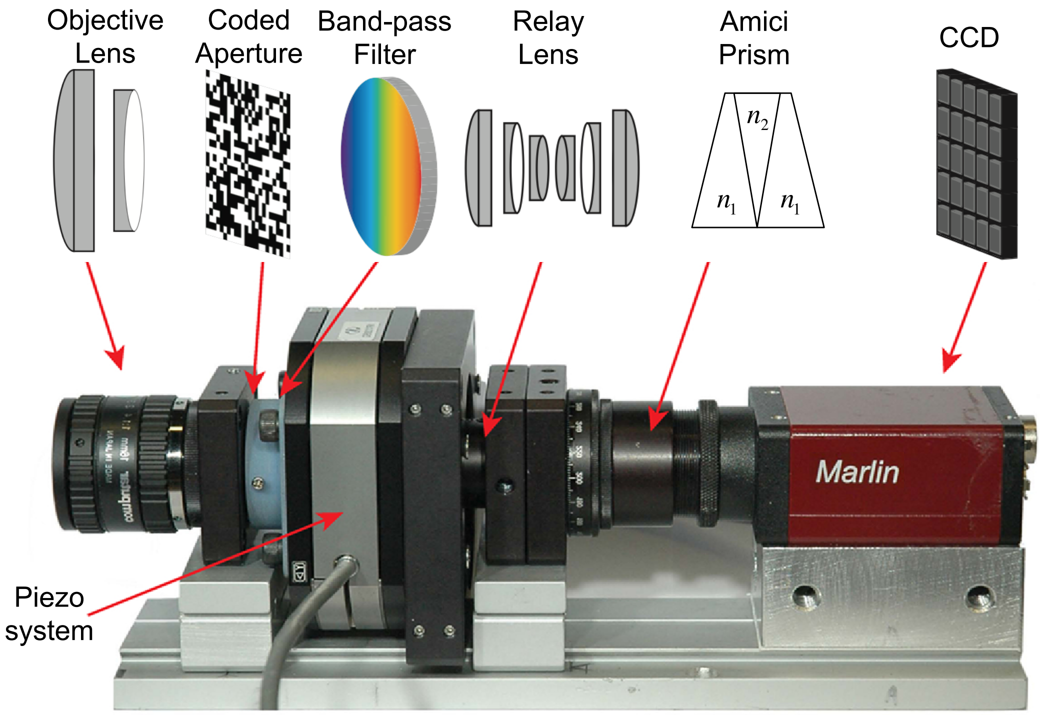

Figure 2.1: CASSI optical architecture proposed in [1].

measured by the FPA detector elements. It can be shown that if the band-pass filter of the instrument limits the spectral components between λ_1 and λ_2, then the number of resolvable spectral band is limited by $L = (\alpha(\lambda_2 - \lambda_1))/\Delta$, where $\alpha\lambda$ is the dispersion induced by the prism and Δ is the pixel pitch in both, the detector and the coded aperture.

2.2 CASSI System Model

Let $f_0(x, y, \lambda)$ be the spatio-spectral power source density, where x and y index the spatial coordinates and λ indexes the wavelength. The spatio-spectral image source density $f_0(x, y, \lambda)$ is firstly spatially coded by a coded aperture $T(x, y)$, resulting in the coded field,

$$f_1(x, y, \lambda) = T(x, y)f_0(x, y, \lambda). \tag{2.1}$$

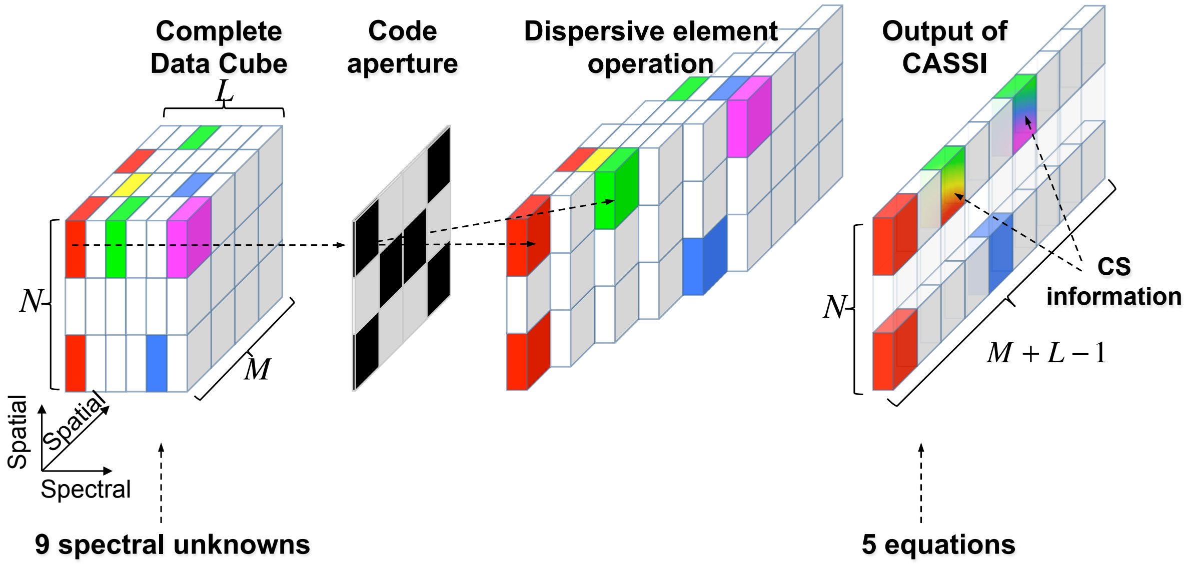

Figure 2.2: Light propagation through the CASSI architecture

The coded aperture transmission function can be written as,

$$T(x,y) = \sum_{i,j} t_{i,j} \mathrm{rect}\left(\frac{x}{\Delta_c} - i, \frac{y}{\Delta_c} - j\right), \tag{2.2}$$

for $i = 1,\ldots,M$, and $j = 1,\ldots,N$, where $M \times N$ is the spatial resolution of the coded aperture, $t_{i,j} \in \{0,1\}$ represents a translucent (1) or a blocking (0) element, and Δ_c is the pixel size of the coded aperture.

The resulting coded field $f_1(x,y,\lambda)$ is subsequently dispersed by a dispersive element before it impinges onto the FPA detector. The spectral density at the output of the dispersive element, can be expressed as,

$$f_2(x,y,\lambda) = \int\int T(x',y') f_0(x',y',\lambda)\delta(x' - x - S(\lambda), y' - y)dx'dy', \tag{2.3}$$

where $\delta(x' - x - S(\lambda), y' - y)$ represents the optical impulse response of the system, such that $S(\lambda) = \alpha(\lambda)(\lambda - \lambda_c)$ is the dispersion induced by the prism along the x-axis, which is centered at the wavelength λ_c and has a dispersion coefficient $\alpha(\lambda)$. The resulting intensity image at the FPA is the integration of the field $f_2(x,y,\lambda)$ over the detector's spectral range sensitivity (Λ) that can be represented as,

$$
\begin{aligned}
g(x,y) &= \int_{\Lambda} f_2(x,y,\lambda)d\lambda, && (2.4)\\
&= \int_{\Lambda}\int\int T(x',y')f_0(x',y',\lambda)\delta(x'-x-S(\lambda),y'-y)dx'dy'd\lambda, && (2.5)\\
&= \int_{\Lambda} T\left(x+S(\lambda),y\right) f_0\left(x+S(\lambda),y,\lambda\right) d\lambda && (2.6)
\end{aligned}
$$

where the last step follows from the assumption that ideal optical elements are used.

Using a first order discretization model [1, 14, 19], a CASSI measurement at the $(m,n)^{th}$ pixel is given by,

$$g_{mn} = \int\int p(m,n;x,y)g(x,y)dxdy + w_{mn}, \quad (2.7)$$

where w_{mn} represents additive noise and,

$$p(m,n;x,y) = \text{rect}\left(\frac{x}{\Delta_d}-m,\frac{y}{\Delta_d}-n\right), \quad (2.8)$$

accounts for the detector pixelation, with Δ_d being the detector pixel pitch, for $m = 1,\ldots,M$, $n = 1,\ldots,N+L-1$, where $M\times N+L-1$ is the FPA spatial resolution. Using Eq. (2.2) and Eq. (2.6), the discrete measurement of the CASSI system can be written as,

$$
\begin{aligned}
g_{mn} &= \iint p(m,n;x,y)g(x,y)dxdy + w_{mn} && (2.9)\\
&= \iiint_{\Lambda} T\left(x+S(\lambda),y\right) f_0\left(x+S(\lambda),y,\lambda\right)\text{rect}\left(\frac{x}{\Delta_d}-m,\frac{y}{\Delta_d}-n\right) d\lambda dxdy && (2.10)\\
&= \iiint_{\Lambda} \sum_{i,j} t_{i,j}\text{rect}\left(\frac{x}{\Delta_c}-i,\frac{y}{\Delta_c}-j\right) f_0\left(x+S(\lambda),y,\lambda\right)\\
&\qquad \times\text{rect}\left(\frac{x}{\Delta_d}-m,\frac{y}{\Delta_d}-n\right) d\lambda dxdy && (2.11)\\
&= \sum_k t_{i-k,j}f_{i-k,j,k}, && (2.12)
\end{aligned}
$$

where the last step follows from the fact that $f_{i,j,k} = \iiint_{\Omega_{ijk}} f_0(x, y, \lambda)dxdyd\lambda$ is the energy of the $(i, j, k)^{th}$ data cube voxel bounded by Ω_{ijk}, and $k = 1, \ldots, L$ indexes the data cube spectral bands.

In matrix form, Eq. (2.12) can be expressed as,

$$\mathbf{g} = \mathbf{Hf}, \tag{2.13}$$

where the $\mathbf{H}$ matrix represents the CASSI sensing process accounting for the CASSI optical elements operation on the discretized datacube. Assuming a $M \times N \times L$ data cube as in Fig. 2.2, a prism exhibiting linear dispersion, shift horizontally each spectral band along x-axis by one pixel each, causing the power spectral density impinges into $M(N + L - 1)$ FPA pixels. Then, CASSI sensing matrix $\mathbf{H}$ is of size $M(N + L - 1) \times MNL$. Hence, a data cube reconstruction $\hat{\mathbf{f}}$ in CASSI relies on the solution of an under-determined ill-posed equations system.

The CASSI system can accept multiple-shot methodologies, where each snapshot exhibits a new coded aperture. Multiple-snapshot sensing entails the knowledge of new information missed in the first snapshots, then attaining higher reconstruction estimations. In particular, letting the i^{th} coded aperture be denoted as $T^i(x, y)$, the i^{th} snapshot can be written as,

$$\mathbf{g}^i = \mathbf{H}^i\mathbf{f}, \tag{2.14}$$

where $\mathbf{H}^i$ is the system transfer function of the CASSI system when the i^{th} coded aperture is used. Arranging K independent snapshots entail the full system transfer function of the CASSI system, which is given by,

$$\mathbf{g} = \mathbf{Hf} = \begin{bmatrix} \mathbf{H}^1 \\ \mathbf{H}^2 \\ \vdots \\ \mathbf{H}^K \end{bmatrix} \mathbf{f}. \tag{2.15}$$

Figure 2.3 presents the system transfer function matrix $\mathbf{H}$ for an input scene of spatial resolution $N = M = 6$, and $L = 5$ spectral bands. There, it can be noticed that as the spectral band increases, it is shifted down by N rows each, and that every new snapshot entails the vertical concatenation of the corresponding transfer function.

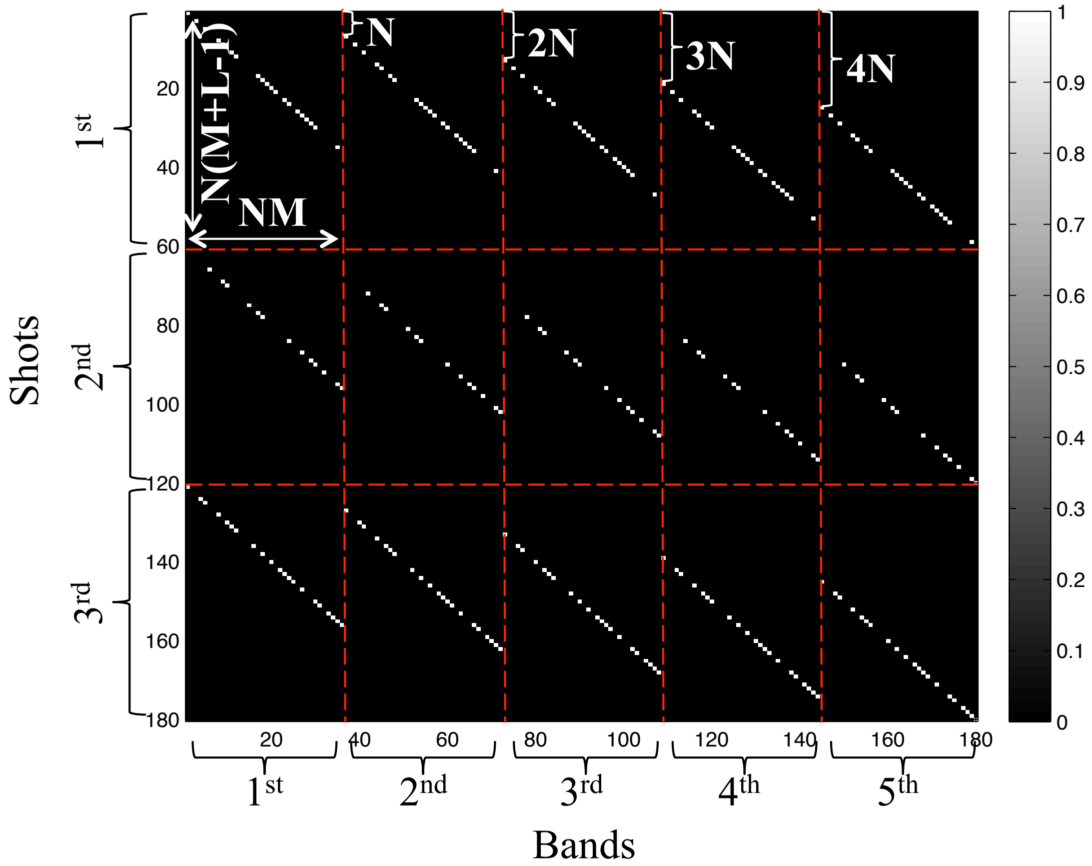

Figure 2.3: Structure of the matrix $\mathbf{H}$ for a $N = M = 6$, $L = 5$ datacube, when $K = 3$ for the CASSI traditional model ($\mathbf{H} \in \mathbb{R}^{180\times180}$). Notice that entries are either 0 or 1.

2.3 Reconstruction Process in CASSI

CASSI datacube reconstructions uses the measurement $\mathbf{g}$ and an estimation of $\mathbf{H}$ matrix. Due to the number of pixels on the detector used for the measurement is smaller than the number of voxels in the discrete data cube, the equations system depicted in Eq. (2.13) is under-determined. CS dictates that one can recover spectral scenes from far fewer measurements than that required by conventional linear scanning spectral sensors. To make this possible, CS relies on two principles: sparsity, which characterizes the spectral scenes of interest, and incoherence, which shapes the sensing structure [15, 16]. Sparsity indicates that spectral images found in nature can be concisely represented in some basis, with just a small number of coefficients. This is indeed the case in spectral imaging where natural scenes exhibit correlation among adjacent pixels and also across spectral bands [18]. Incoherence refers to the structure of the sampling waveforms used in CS, which, unlike the signals of interest, have a dense representation in the basis [17]. The remarkable discovery behind CS is that it is possible to design sensing protocols capable of capturing the essential information content in sparse signals with just a small number of compressive measurements. The sensing modality simply correlates incoming signals with a small number of fixed waveforms that satisfy the incoherence principle. The signals of interest are then accurately reconstructed from the small number of compressive measurements by numerical optimization [15, 17, 19].

Let represent the spectral data cube $\mathbf{f}$ in an orthonormal basis as,

$$\mathbf{f} = \mathbf{\Psi}\boldsymbol{\theta}, \tag{2.16}$$

where $\boldsymbol{\theta}$ is the sparse coefficients representation of the data cube on the basis $\mathbf{\Psi}$. Then, the compressive FPA measurements are given by,

$$\mathbf{g} = \mathbf{H}\mathbf{\Psi}\boldsymbol{\theta}. \tag{2.17}$$

In this way, a hyperspectral image data cube reconstruction $\hat{\mathbf{f}}$ for CASSI can be attained by solving the CS-based optimization problem,

$$\hat{\mathbf{f}} = \mathbf{\Psi}^T\{\text{argmin}_{\boldsymbol{\theta}'}\|\mathbf{g} - \mathbf{H}\mathbf{\Psi}\boldsymbol{\theta}'\|_2^2 + \tau\|\boldsymbol{\theta}'\|_1\} \tag{2.18}$$

where $\tau > 0$ is a regularization parameter that balances the conflicting tasks of minimizing the least square of the residuals, while at the same time, yielding a sparse solution. Figure 2.4 shows an sketch of the reconstruction procedure performed to recover an estimation of the input spectral data cube $\mathbf{f}$, from K snapshots of the CASSI.

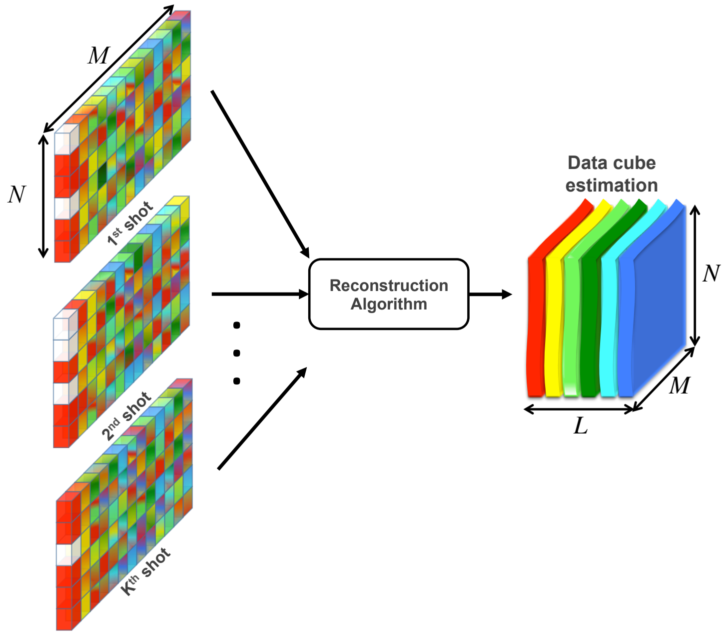

Figure 2.4: Sketch of the reconstruction process of compressive spectral images. The set of K snapshots and the $\mathbf{H}$ matrix are used to obtain an estimation of the data cube.

Chapter 3

HIGHER-ORDER MODEL FOR COMPRESSIVE SPECTRAL IMAGING

3.1 Proposed Discretization Process

Using a first order discretization model [1, 14, 19], a CASSI measurement is given as stated in Eq. 2.7. This approximation however is coarse, leading to inter-pixel blurring in the detection. The goal of this thesis is thus to develop a more precise, higher order computational model that mitigates the inter-voxel interference, which in turn leads to higher quality spectral imaging. At the same time, the higher-order precision model allows less reliance on calibration corrections. To this end, the pixelation function $p(m,n;x,y)$ is replaced by defining the integration limits at the detector as,

$$g_{mn} = \int_{n\Delta}^{(n+1)\Delta} \int_{m\Delta}^{(m+1)\Delta} \int_{\Lambda} T(x - S(\lambda), y) f_0(x - S(\lambda), y, \lambda) d\lambda dx dy, \tag{3.1}$$

and the new discretization model is then derived as follows. The source $f_0(x,y,\lambda)$ is discretized as the signal f_{ijk} where i, j, and k are the discrete indices accounting for x, y, and λ respectively. A voxel f_{ijk} represents the intensity concentrated in a specific spatio-spectral region Ω_{ijk} where $x \in [i\Delta, (i+1)\Delta]$, $y \in [j\Delta, (j+1)\Delta]$, and $\lambda \in [\lambda_k, \lambda_{k+1}]$. Specifically, the $(ijk)^{th}$ voxel is given by

$$\begin{aligned} f_{ijk} &= \int\limits_{\lambda_k}^{\lambda_{k+1}} \int\limits_{j\Delta}^{(j+1)\Delta} \int\limits_{i\Delta}^{(i+1)\Delta} f_0(x,y,\lambda) dx dy d\lambda \qquad (3.2) \\ &= \iiint\limits_{\Omega_{ijk}} f_0(x,y,\lambda) dx dy d\lambda = c_{ijk} \cdot f_0(x_i, y_j, \lambda_k), \end{aligned}$$

where c_{ijk} represents the quadrature weight, and x_i, y_j, and λ_k are average values in Ω_{ijk}. Notice in (3.2) that the spectral axis λ has been discretized in L spectral bands. The range of the k^{th} spectral band is $[\lambda_k \ \lambda_{k+1}]$ where λ_k is the solution to the equation given by

$$S(\lambda_k) - S(\lambda_0) = k\Delta, \quad k = 0, \dots, L-1, \tag{3.3}$$

where again $S(\lambda) = \alpha(\lambda)(\lambda - \lambda_c)$ is the dispersion of the prism. Equation (3.3) establishes that the spectral axis resolution is determined by the prism response $S(\lambda)$ and by the pitch of the detector Δ. Equation (3.2) also establishes the spatial resolution which is determined by the pitch of the detector Δ that is assumed to be equal to the coded aperture pitch. Using the ranges of the L spectral bands defined in (3.3), Eq. (3.1) can be expressed as

$$g_{mn} = \int_{n\Delta}^{(n+1)\Delta} \int_{m\Delta}^{(m+1)\Delta} \left[\sum_{k=0}^{L-1} \int_{\lambda_k}^{\lambda_{k+1}} T(x - S(\lambda), y) f_0(x - S(\lambda), y, \lambda) d\lambda \right] dx dy. \tag{3.4}$$

To better illustrate the discretization of the source, Fig. 3.1 depicts the physical phenomena described in Eq. (3.4). Notice that each cubic voxel when sheared by the prism effects, turns into an oblique voxel. The oblique voxel is stretched along the x axis, such that when it is projected onto the detector grid, it impinges onto several detector pixel elements at once. Hence, several voxels at the source will impact each of the FPA pixels.

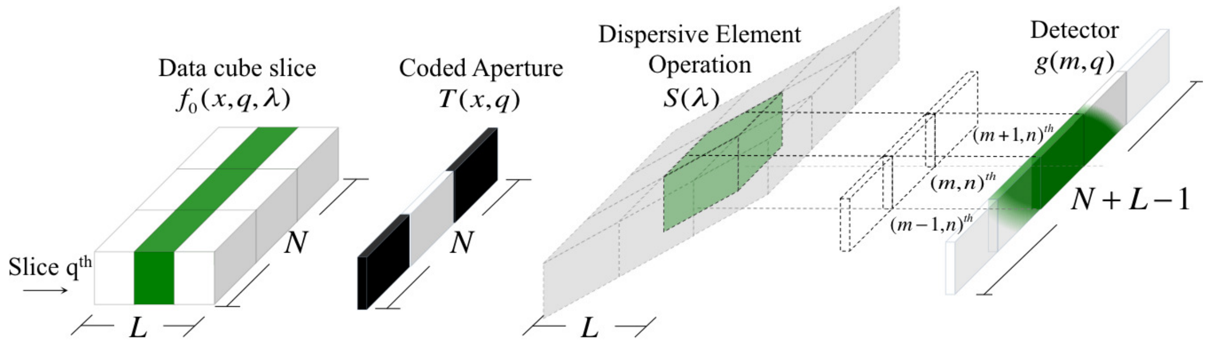

Figure 3.1: CASSI integration model. A voxel of the data cube is coded by the aperture code, sheared by the dispersive element with dispersion $S(\lambda_k)$ and projected onto several pixels of the detector.

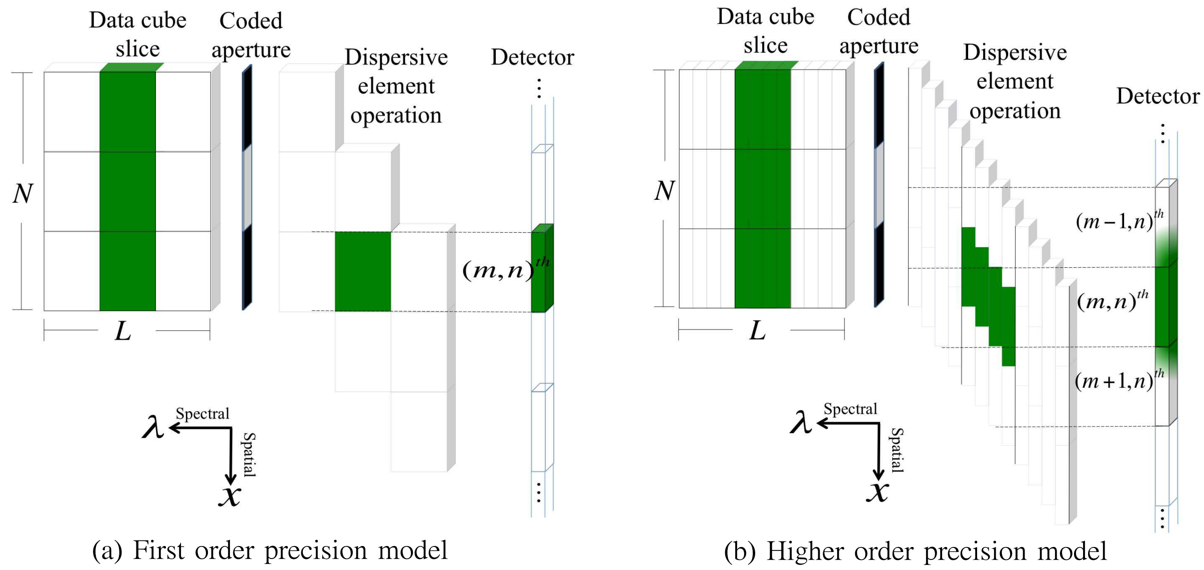

Figure 3.2: (a) First order discretization model. A voxel impinges onto a single FPA pixel detector; (b) higher order discretization model. A voxel impinges onto three FPA pixels. Notice that the light dispersion path is on the (λ, x) axis (top view).

The inter-voxel interference is next examined by two discretization models as illustrated in Fig. 3.2, when viewed from the top of the datacube. A linear dispersive function with slope equal to one ($d_S = 1$) is assumed in the figure. Figure 3.2(a) depicts the traditional discretization approach proposed in [1]. Figure 3.2(b) shows the higher precision discretization model where the FPA pixel detector captures energy from several voxels simultaneously. The dotted lines indicate the spatio-spectral region of the data cube integrated in the $(m, n)^{th}$ detector pixel. It can be observed that the higher precision discretization of the dispersive curve leads to more voxels superimposing in the formation of g_{mn}.

Figure 3.3 shows a zoomed version of just one voxel of the source after it is sheared by the prism. Notice that its energy will impinge on up to three different FPA pixels when $d_S = 1$. Each voxel at the source can then be partitioned into three different regions denoted as R_0, R_1, and R_2. Depending on the nature of $S(\lambda)$, a voxel may affect from 2 as depicted in Fig. 3.4 up to more than 3 detector elements. Therefore, for a

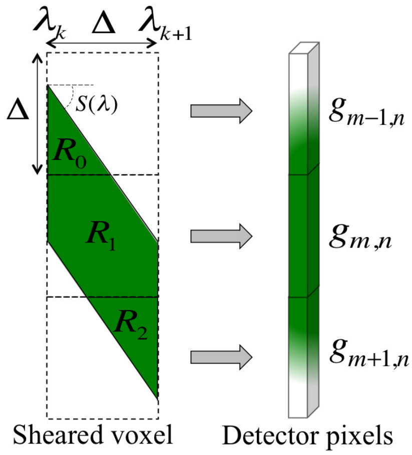

Figure 3.3: A voxel dispersed into the regions R_0, R_1, and R_2 in each interval $[\lambda_k\ \lambda_{k+1}]$. These regions determine the voxel fractions involved in the formation of the $g_{m-1,n}$, $g_{m,n}$ and $g_{m+1,n}$ detector pixels.

general dispersion curve, each of the integrals in Eq. (3.4) can be rewritten as

$$\iiint\limits_{n\Delta,m\Delta,\lambda_k}^{(n+1)\Delta,(m+1)\Delta,\lambda_{k+1}} T(x-S(\lambda),y)f_0(x-S(\lambda),y,\lambda)d\lambda dxdy = \sum_{u=0}^{d} \int\limits_{\lambda_k}^{\lambda_{k+1}}\iint\limits_{\{x-S(\lambda),y\}\in R_u} T(x-S(\lambda),y)f_0(x-S(\lambda),y,\lambda)dxdyd\lambda, \tag{3.5}$$

where $d = d_S + 1$ for linear dispersion, and $d = \max\lceil(m+1)\Delta - S(\lambda_k)\rceil$ when a prism exhibits a non-linear response. Further, let the discrete version of the aperture code $T(x,y)$ be $t_{i,j}$ and using the representation in Eq. (3.2) for $f_0(x,y,\lambda)$, then

$$\int\limits_{\lambda_k}^{\lambda_{k+1}} \iint\limits_{\{x-S(\lambda),y\}\in R_u} T(x-S(\lambda),y)f_0(x-S(\lambda),y,\lambda)dxdyd\lambda = w_{mnku}t_{(m-k-u)n}f_{(m-k-u)nk} \tag{3.6}$$

where the proportion of the voxel $f_{(m-k-u)nk}$ contained in R_u is taken into account by the constant w_{mnku}. Notice that the subindex k in w_{mnku} refers to the spectral interval $[\lambda_k\ \lambda_{k+1}]$. While the weights w_{mnku} can be estimated using a calibration process, they can also be numerically approximated assuming that the the spectral information is uniformly

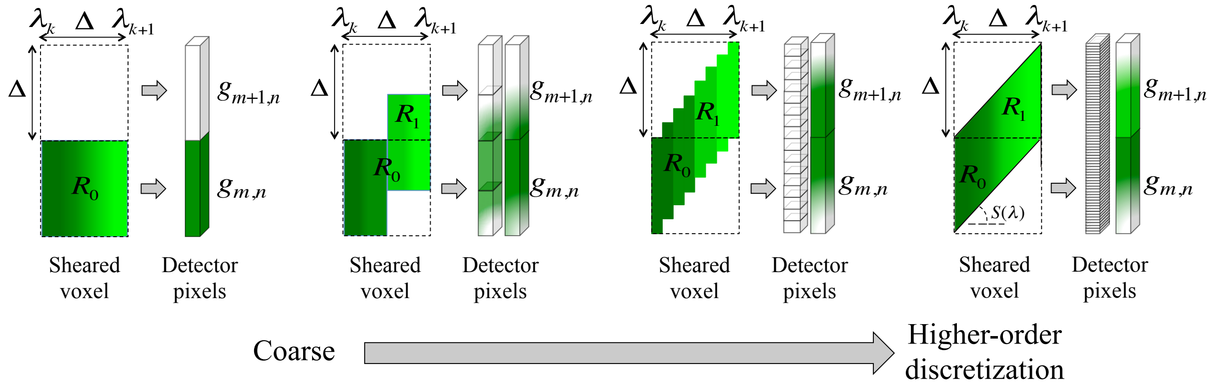

Figure 3.4: Discretization of the dispersion of a single voxel of the data cube as we go from a coarse to a finner discretization.

distributed in the region delimited by Ω_{ijk}. More specifically, they are calculated as

$$w_{mnku} = \left(\iiint_{R_u} dxdyd\lambda \right) \left(\iiint_{\Omega_{(m-k-u)nk}} dxdyd\lambda \right)^{-1} \tag{3.7}$$

where R_u is taken in the respective interval $[\lambda_k \; \lambda_{k+1}]$. In practice, the sections R_u can be calculated by estimating the prism response $S(\lambda)$ and the misalignment between the coded aperture and the FPA detector. Using Eq. (3.5) and (3.6), Eq. (3.4) can be expressed as

$$g_{mn} = \sum_{k=0}^{L-1} \sum_{u=0}^{d} w_{mnku} t_{(m-k-u)n} f_{(m-k-u)nk}. \tag{3.8}$$

3.2 Higher Order Discrete Matrix Model

Equation (3.8) can be written in matrix form as $\mathbf{g} = \mathbf{Hf}$, where the $N(N+L+d-1)$ long vector $\mathbf{g}$ and the N^2L long vector $\mathbf{f}$ represent the compressive measurements and the spectral data cube respectively, ordered lexicographically. When several FPA measurements are captured each one using a different aperture code, the i^{th} FPA measurement can be written as

$$\mathbf{g}_i = \mathbf{H}_i\mathbf{f}. \tag{3.9}$$

In Eq. (3.9) each $N(N+L+d-1) \times N^2L$ matrix $\mathbf{H}_i$ is composed by,

$$\mathbf{H}_i = \mathbf{P}\mathbf{T}_i, \tag{3.10}$$

where $\mathbf{P}$ accounts for the weights w_{mnku} and the dispersion of the prism, and $\mathbf{T}_i$ represents the i^{th} coded aperture. Here $\mathbf{T}_i$ is a block-diagonal matrix of the form,

$$\mathbf{T}_i = \begin{bmatrix} \text{diag}(\mathbf{t}_i) & \mathbf{0}_{N^2} & \cdots & \mathbf{0}_{N^2} \\ \mathbf{0}_{N^2} & \text{diag}(\mathbf{t}_i) & \cdots & \mathbf{0}_{N^2} \\ \vdots & \vdots & \ddots & \vdots \\ \mathbf{0}_{N^2} & \mathbf{0}_{N^2} & \cdots & \text{diag}(\mathbf{t}_i) \end{bmatrix}, \tag{3.11}$$

where $\mathbf{t}_i$ is the i^{th} aperture code in lexicographical notation and $\mathbf{0}_{N^2}$ is a $N^2 \times N^2$ zero-matrix. Notice that Eq. (3.7) can be written in matrix form as, $(\mathbf{W}_k^u)_{mn} = \omega_{mnku}$, for $m, n = 0, 1, \ldots, N-1$, and k, u as in Eq. (3.8). Then, the matrix $\mathbf{P}$ is given by $\mathbf{P} = \sum_{u=0}^{d} \mathbf{P}_u$, such that

$$\mathbf{P}_u = \begin{bmatrix} \multicolumn{4}{c}{\mathbf{0}_{Nu \times N^2L}} \\ \text{diag}(\mathbf{W}_0^u) & \mathbf{0}_{N \times N^2} & \cdots & \mathbf{0}_{N \times N^2} \\ \mathbf{0}_{N \times N^2} & \text{diag}(\mathbf{W}_1^u) & \cdots & \mathbf{0}_{N \times N^2} \\ \vdots & \vdots & \ddots & \vdots \\ \mathbf{0}_{N \times N^2} & \mathbf{0}_{N \times N^2} & \cdots & \text{diag}(\mathbf{W}_{L-1}^u) \\ \multicolumn{4}{c}{\mathbf{0}_{N(d-u) \times N^2L}} \end{bmatrix}. \tag{3.12}$$

The ensemble of measurements $\{\mathbf{g}_i\}_{i=1}^K$, can be succinctly written as $\boldsymbol{g} = \tilde{\mathbf{H}}\mathbf{f} = \boldsymbol{\mathcal{P}}\boldsymbol{\mathcal{T}}\mathbf{f}$, where $\boldsymbol{g} = \left[\mathbf{g}_1^T, \ldots, \mathbf{g}_K^T\right]^T$, $\boldsymbol{\mathcal{P}}$ is a K-times block-diagonal matrix of $\mathbf{P}$, and $\boldsymbol{\mathcal{T}} = \left[\mathbf{T}_1^T, \ldots, \mathbf{T}_K^T\right]^T$, with K representing the number of FPA shots. Figure 3.5 depicts the structure of the matrix $\tilde{\mathbf{H}}$ for the first order and the higher order discretization models, when three FPA shots are used to capture a $6 \times 6 \times 5$ datacube.

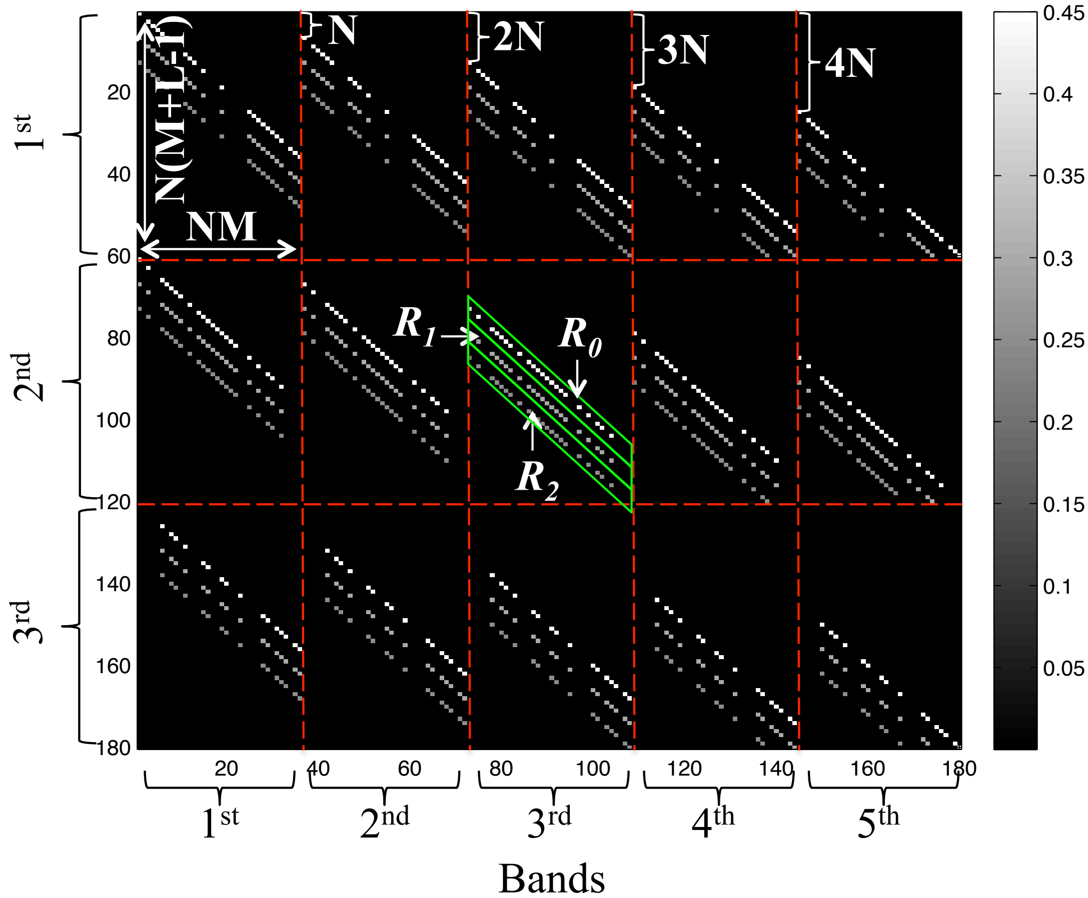

Figure 3.5: Structure of the matrix $\tilde{\mathbf{H}}$ for a $N = M = 6$, $L = 5$ datacube, when $K = 3$ for the higher order CASSI model ($\tilde{\mathbf{H}} \in \mathbb{R}^{180\times180}$). Extra diagonal terms account for the inter-voxel interference. Notice that entries of the $\mathbf{H}$ matrix in Fig. 2.3 are either 0 or 1, while they vary in the interval [0, 1] for the higher-order model.

Chapter 4

SIMULATION RESULTS

In order to compare the higher-order precision model with the traditionally used model, a hyper-spectral data cube was experimentally acquired using a wide-band Xenon lamp as the light source, and a visible monochromator. Monochromatic images were captured every 1nm in the spectral range $\{450-620\}$; thus 170 spectral planes were acquired. The image intensity was captured by a CCD camera AVT Marlin F033B, with 656×492 pixels, exhibiting a pixel pitch of 9.9μm and using 8 bits for pixel depth. In addition, a double Amici prism was used as the dispersive element. Its non-linear dispersion curve shown in Fig. 5.1(b) was determined experimentally by using the monochromator as the input of the setup. Other elements such as the lens, the spectral response of the camera, and the coded apertures are considered ideal. Deviations from the ideal characteristics of these elements are mitigated partially by a calibration step. In this architecture, a voxel spanning any of the following wavelength intervals will create a displacement of a pixel on the detector: $\{450-463\}$, $\{464-477\}$, $\{478-493\}$, $\{494-510\}$, $\{511-530\}$, $\{531-556\}$, $\{557-586\}$ and $\{587-620\}$ where all the intervals are given in nanometres. Thus, the 170 spectral planes of the datacube will be clustered into 8 bands. Notice that the intervals width are not constant, as a non-linear dispersive element was used. Figure 4.1 shows the eight spectral bands of the datacube, which the CASSI system aims at recovering.

Experiments use the multi frame CASSI setup described in [13], and simulation algorithms utilizes 64 bits as arithmetic precision. Aperture codes entries are random realizations of a Bernoulli random variable with parameter $p = 0.5$. Note that the proposed model uses the same pitch for coded aperture features and FPA pixels. In summary, the hyper-spectral test data cube $\mathbf{F}$ has 256×256 pixels of spatial resolution and $L = 8$

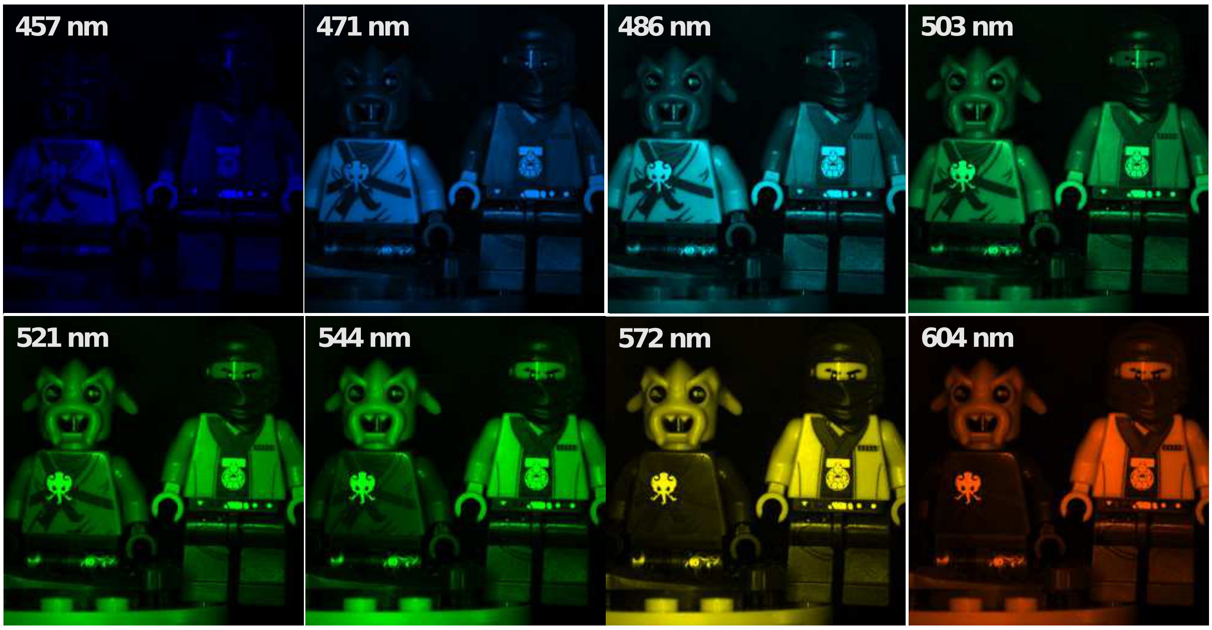

Figure 4.1: Spectral bands used in the simulations and their central wavelength.

spectral bands in the range 450 nm to 620 nm. In order to simulate the analogous sensing process, the compressive measurements are obtained using the 170 spectral planes of the datacube, as shown in Fig. 3.2(b). Notice also that the reconstruction process aims to recover the average of the spectral information in the 8 mentioned spectral intervals. The calibration weights for the proposed model are approximated using Eq. 3.7 and the prism's response curve.

Given the set of compressive measurements, the voxels' weight distribution and the set of coded apertures, the hyper-spectral datacube is recovered using the GPSR algorithm [20]. GPSR exploits the sparse nature of the hyperspectral datacube. In particular, the hyperspectral signal $\mathbf{F} \in \mathbb{R}^{N \times M \times L}$, or its vector representation $\mathbf{f} \in \mathbb{R}^{N.M.L}$, are assumed to be $K-$sparse on some basis $\mathbf{\Psi}_{3D}$, such that $\mathbf{f} = \mathbf{\Psi}_{3D}\boldsymbol{\theta}$, where $\boldsymbol{\theta}$ are the coefficients of the sparse representation. Hence, $\mathbf{f}$ can be approximated by a linear combination of K vectors from $\mathbf{\Psi}_{3D}$ with $K \ll (N.M.L)$. Specifically, this algorithm estimates a hyperspectral datacube $\hat{\mathbf{f}}$ by solving the optimization problem,

$$\hat{\mathbf{f}} = \mathbf{\Psi}_{3D}^{T}\{\text{argmin}_{\boldsymbol{\theta}'}\|\boldsymbol{g} - \boldsymbol{\mathcal{P}}\boldsymbol{\mathcal{T}}\mathbf{\Psi}_{\text{3D}}\boldsymbol{\theta}'\|_2^2 + \tau\|\boldsymbol{\theta}'\|_1\}, \tag{4.1}$$

where $\tau > 0$ is a regularization parameter that balances the conflicting tasks of minimizing the least square of the residuals, while at the same time, it seeks for a sparse solution The basis representation $\mathbf{\Psi}_{3D}$ is set as the Kronecker product of three basis $\mathbf{\Psi}_{3D} = \mathbf{\Psi}_1 \otimes \mathbf{\Psi}_2 \otimes \mathbf{\Psi}_3$, where the combination $\mathbf{\Psi}_1 \otimes \mathbf{\Psi}_2$ is the 2D-Wavelet Symmlet 8 basis and $\mathbf{\Psi}_3$ is the Discrete Cosine basis. The reconstructions are performed using the new model in Eq. (3.8), and the traditional model in Eq. (1.1) with its respective calibration process described in [14]. The regularization parameters needed in the compressive sensing reconstruction algorithm are carefully selected such that each simulation uses the best selectable parameter.

Figure 4.2 shows the PSNR of the reconstructions for the two models as function of the measurement shots. The gain achieved by the new model is quantitatively noticeable by averaging the PSNR of the recovered datacubes. This improvement approaches to 4 dB when more than two FPA shots are used.

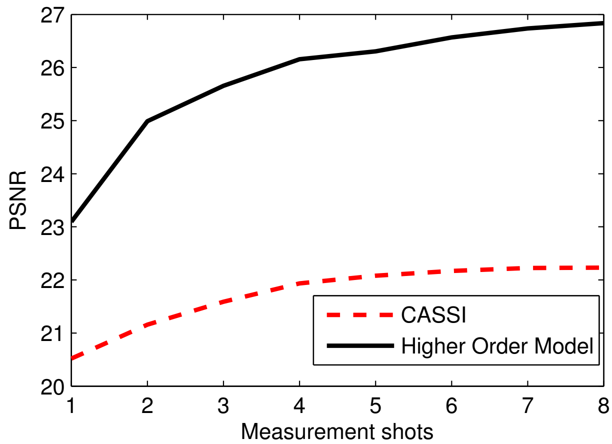

Figure 4.2: Averaged PSNR of the reconstructed datacubes as function of the number of FPA shots. The traditional and the higher order precision models are compared.

Figure 4.3 depicts the reconstructed spectral bands (zoomed area) when 6 shots are captured for the model in (1.1). Figure 4.4 illustrates the reconstruction of the same spectral bands (zoomed area) when the same number of shots are used in the new model. It can be observed that the new model recovers the spectral information with higher accuracy.

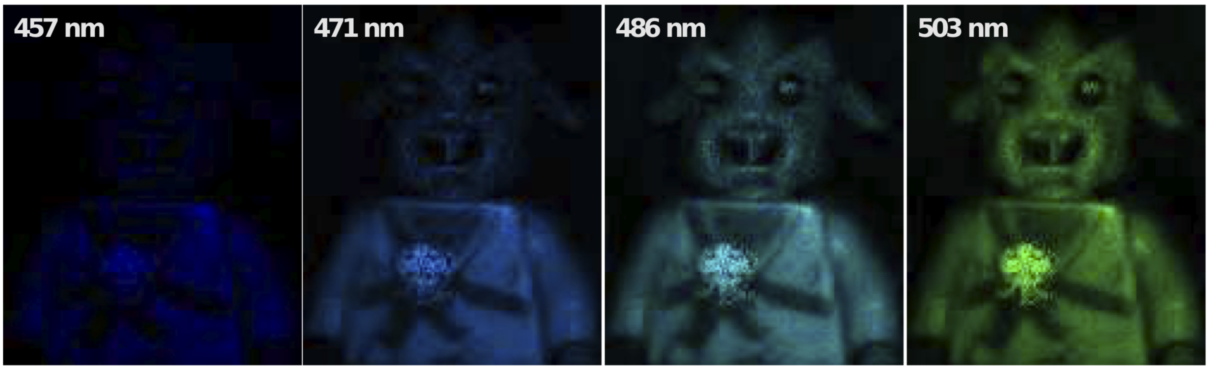

(a) 18.6 dB (b) 23.2 dB (c) 23.7 dB (d) 23.7 dB

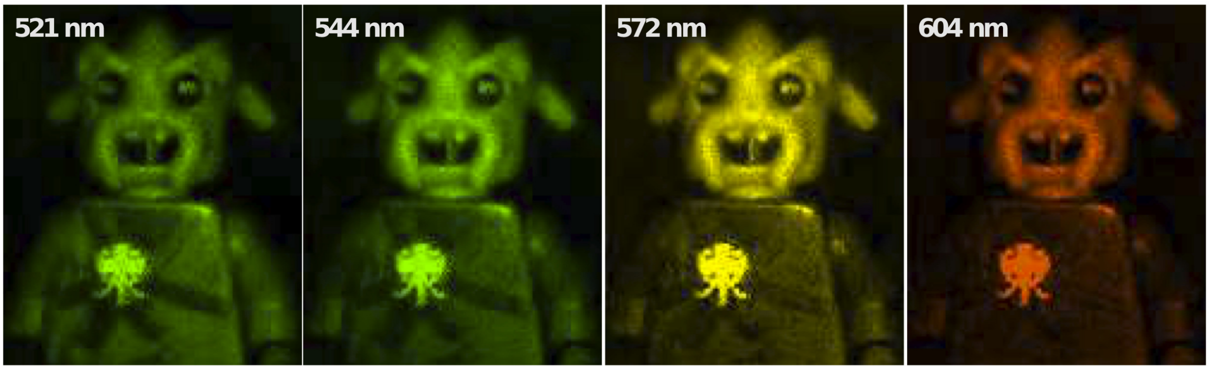

(e) 17.2 dB (f) 23.0 dB (g) 26.4 dB (h) 22.6 dB

Figure 4.3: Reconstruction using the traditional CASSI model and the corresponding attained PSNR. The average PSNR across the 8 bands is 22.3 dB.

(a) 23.5 dB

(b) 25.9 dB

(c) 25.9 dB

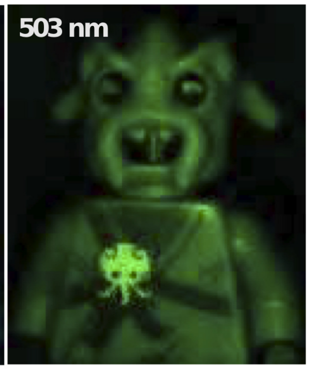

(d) 26.4 dB

(e) 27.9 dB

(f) 28.8 dB

(g) 28.5 dB

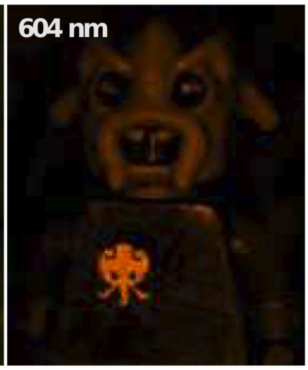

(h) 25.7 dB

Figure 4.4: Reconstruction using the higher order CASSI model and the corresponding attained PSNR. The average PSNR across the 8 bands is 26.85 dB

Chapter 5

EXPERIMENTAL SETUP AND ANALYSIS

The testbed shown in Fig. 5.1(a) is used to implement the CASSI system and to verify the simulation results [13]. It is formed by two subsystems: the first composed by the illuminated target, the objective lens and the DMD; the second by the imaging lenses, the band pass filter, the dispersive element, and the CCD camera. The target is illuminated by a white light source and its reflected light is captured by the objective lens which focuses the light onto the DMD plane, which plays the role of the coded aperture. Afterwards, the reflected light from the DMD is focused by the imaging lenses into the prism imaging plane that disperses the filtered light onto the CCD camera which integrates the underlying 3D hyperspectral image in the 2D FPA.

The testbed setup is characterized in order to reduce the impact of non-linearities, non-uniformities, and external noise artifacts. This process is realized as follows: (a) The light source intensity distribution and the FPA spectral sensitivity are characterized by experimentally analyzing their spectral responses using a USB2000+VIS-NIR Ocean Optics spectrometer with a known spectral response. These non-uniform spectral response curves are taken into account to reduce their impact in the measurement shots; (b) for each one of the 170 captured spectral planes, 10 FPA measurements are captured and averaged to reduce the impact of shot and readout noise; (c) the CCD exposure time is setted to 100 microseconds, in order to improve the signal-to-noise-ratio of the aperture code at each wavelength; (d) the dispersive element is characterized in order to take into account its non-linear response curve and the resultant bandwidth of each spectral band.

After characterization of the testbed and in order to observe the oblique voxel effect impinging into the FPA as explained in Fig. 3.2, a measurement shot is captured using

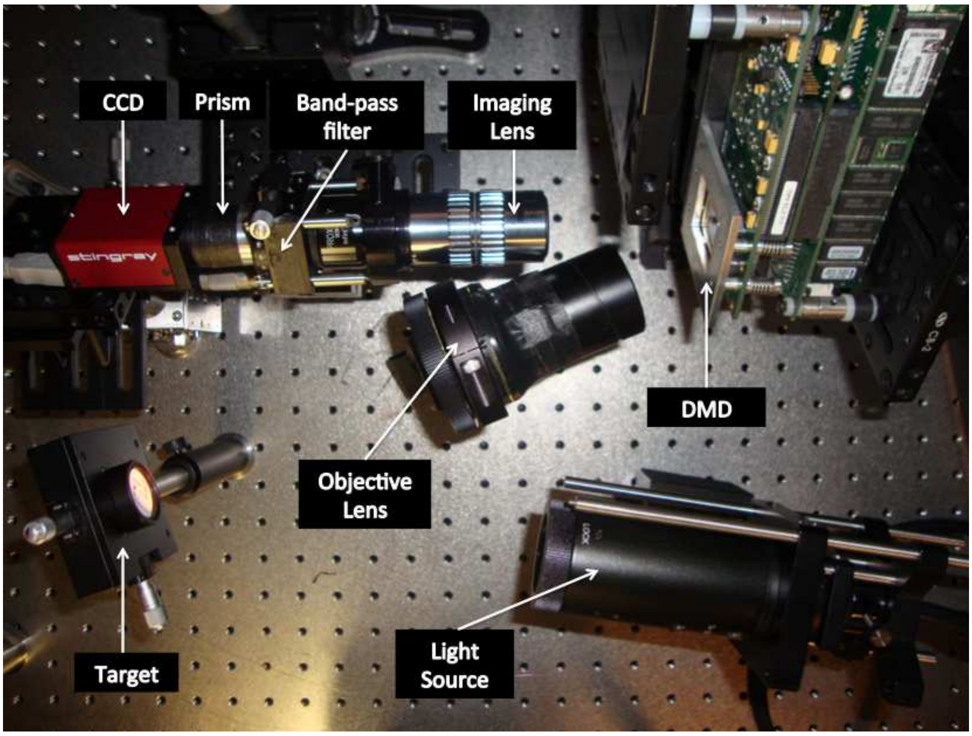

(a)

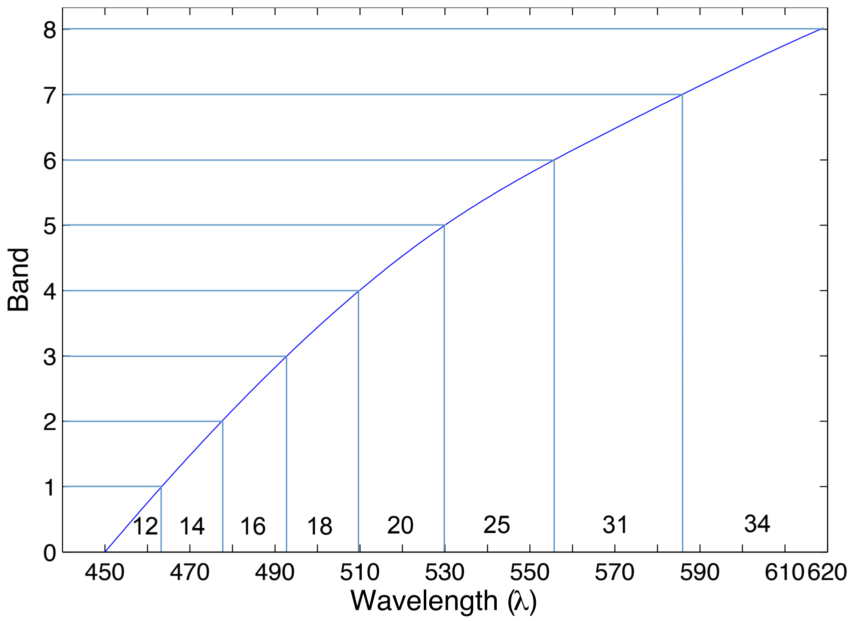

(b)

Figure 5.1: (a) The CASSI testbed setup and its six optical elements: objective lens, DMD, imaging lenses, band-pass filter, prism and CCD; (b) non-linear dispersion response of the Amici prism between $\{450 - 620\}$nm.

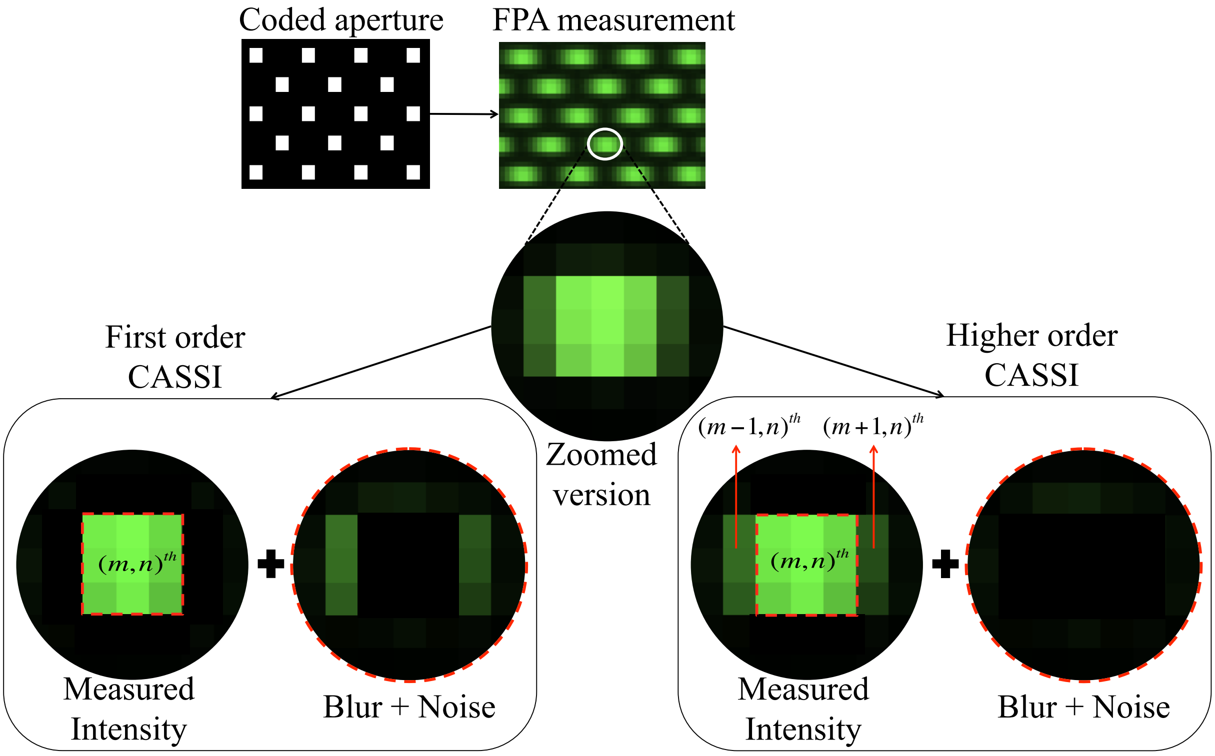

Figure 5.2: FPA measurement at 502 nm. The coded aperture (upper-left) is used in order to isolate the effect of a single voxel impinging onto the FPA (upper right). A zoomed version of a single FPA pixel shows the measured intensity taken into account for each of the discretization models. The energy classified as noise and blur by the first order and the higher order models, is shown.

monochromatic light at 502 nm as the input of the system. The resultant measurement is depicted in Fig. 5.2. This measurement is taken using a test coded aperture with enough space (3 'off' features) between each 'on' feature, thus, allowing the isolation of the effect of a single voxel impinging onto the FPA. Then, a zoomed version of a single FPA pixel is analyzed. Firstly, it can be confirmed that energy belonging to a single datacube voxel impinges principally in a single FPA pixel $(m,n)^{th}$, and a smaller portion is projected into its neighbors $(m-1,n)^{th}$ and $(m+1,n)^{th}$. Second, the first order model accounts only for the energy impinging on the principal pixel, discarding the energy around it, or classifying it as noise or blur. The energy discarded by the first order model, is taken into account in the higher order model by the weights w_{mnku}. Notice that the energy considered as noise and blur by the traditional CASSI is leveraged by the use of a calibration cube at the reconstruction stage, while the proposed model finds the weights distribution in an off-line process. Then, the proposed higher-precision computational model becomes more suitable for reconfigurable multi-shot CASSI where multiple coded apertures are used sequentially.

For experimental purposes, two objective scenes are used and depicted in Fig. 5.3. The coded apertures are realizations of a Bernoulli random variable with $p = 0.5$, realized by a DMD as explained in [13] exhibiting 128×128 pixels. The dispersive element is an Amici prism exhibiting the non-linear response shown in Fig. 5.1(b). To match with the pitch of the coded aperture features and accounting for the dispersion process, 128×136 pixels of the CCD are required. The weight distribution extraction is performed using Eq. (3.7). As a result, three $128 \times 128 \times 8$ weight datacubes were obtained, each one accounting for the regions R_0, R_1 and R_2 as described in Fig. 5.4. By averaging each weight datacube per band, a succinctly version can be shown in Table 5.1. Notice that when misalignments between the coded aperture and the FPA occur, the weights distributions may vary along the regions.

Figure 5.3: Objects in scene used in the experimental comparison

The GPSR algorithm is employed in the reconstruction of the underlying hyper-spectral scene, with parameters as described in the simulations section [20]. Figures 5.5 and5.7 depict the 8 reconstructed spectral bands for $K = 6$ snapshots when the models in Eq. (1.1) and Eq. (3.8) are used for the 2 test targets, respectively. Here, the higher quality reconstruction obtained when the proposed model is used in the simulations section is confirmed. Notice that the test objects intensity spans principally along the

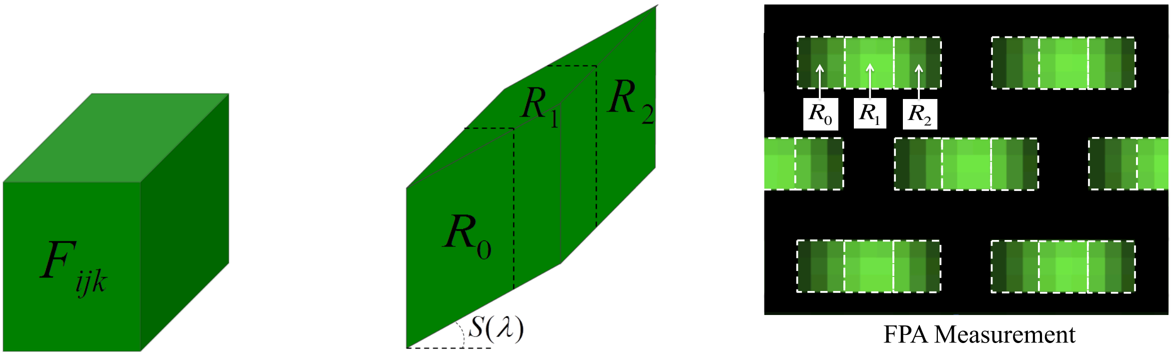

Figure 5.4: Weights estimation for a single voxel. The voxel F_{ijk} is sheared by the dispersive element, such that the voxel is devided into 3 regions R_0, R_1, R_3 which are differentiated in the FPA. The resulting weights are shown in Table 5.1.

Region	Band							
	1	2	3	4	5	6	7	8
R_0	0.30	0.27	0.27	0.26	0.26	0.25	0.24	0.24
R_1	0.42	0.46	0.46	0.49	0.52	0.55	0.56	0.56
R_2	0.28	0.27	0.27	0.25	0.22	0.20	0.20	0.20

Table 5.1: Weights R_i and their distribution across spectral bands. Notice that the weights are non-constant due to the non-linearity of the prism.

last four bands, and the reconstruction quality of the proposed model overcomes the one from the traditional CASSI model. In particular, the improvement can be clearly noticed in the fifth bands (524 nm), where the higher-order CASSI estimates a better shape of the Lego chest, and similarly, the butterfly, compared with the same band resulting from the traditional CASSI model. Furthermore, the improved results can also be noticed in the spectral signatures of two particular points (P1 and P2) depicted in Fig. 5.6 and Fig. 5.8, for the 2 different target toys, respectively. The resulting reconstructed data cube curves are compared against their respective ground truth curves measured by the use of the commercially spectrometer. It can be seen that the signatures obtained with the higher-order model, proposed in this thesis, fit better to the ground truth references, independently of the image target scene analyzed, and also independently of the points chosen to be analyzed.

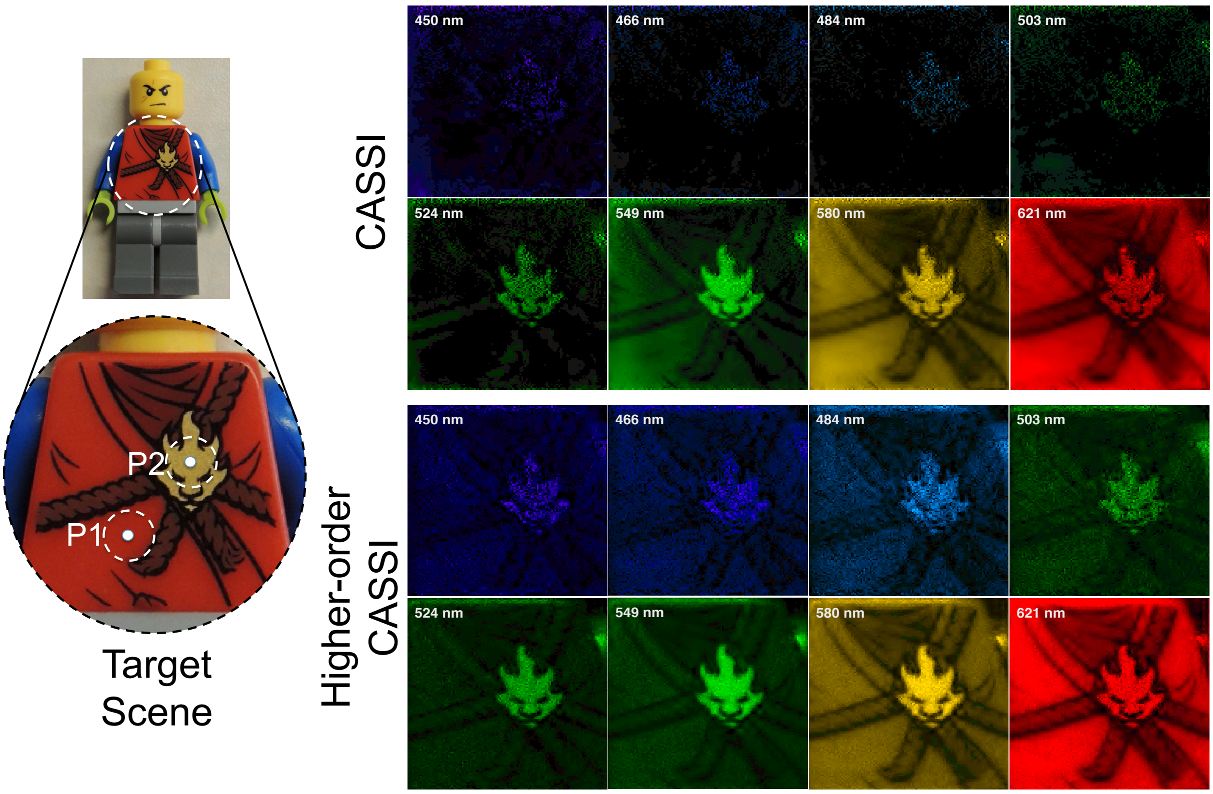

Figure 5.5: Reconstruction of the 8 spectral bands using (a) the traditional CASSI model, and (b) the proposed higher-order CASSI model.

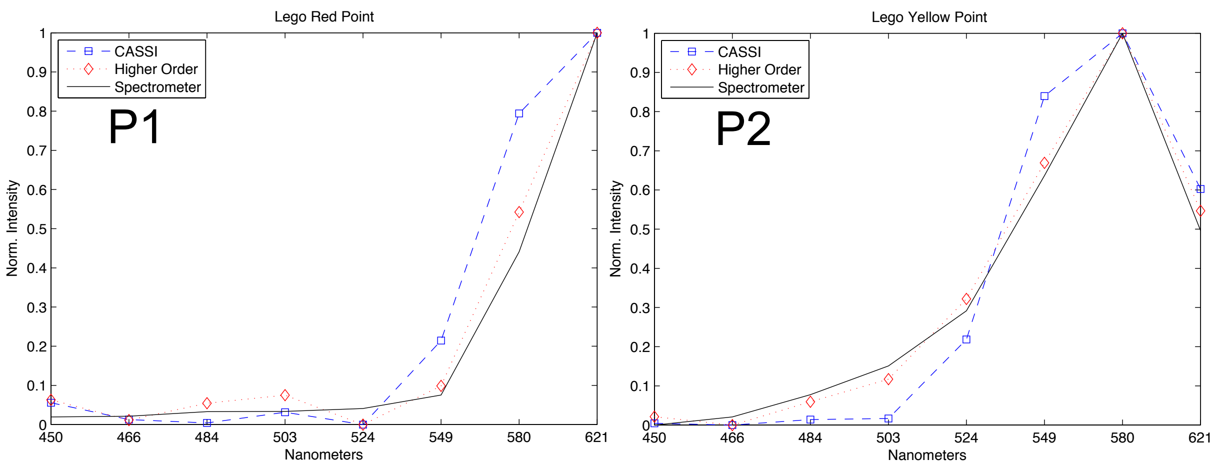

Figure 5.6: Spectral signatures comparison from given points in Fig. 5.5.

It is important to point out here, that the simulations setup differs from the experimental setup in the following aspects: The former performs the CASSI and higher-order CASSI FPA measurements starting with a hyperspectral datacube captured off-line and

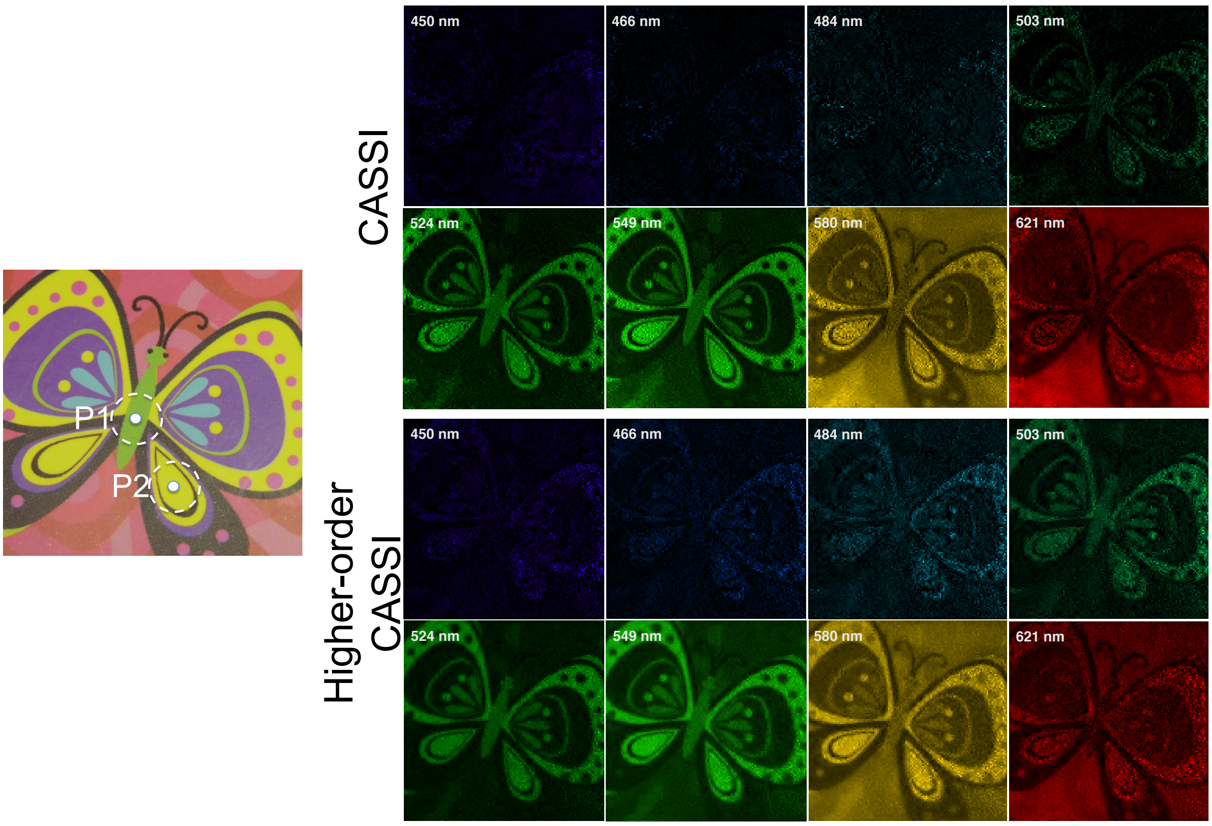

Figure 5.7: Reconstruction of the 8 spectral bands using (a) the traditional CASSI model, and (b) the proposed higher-order CASSI model.

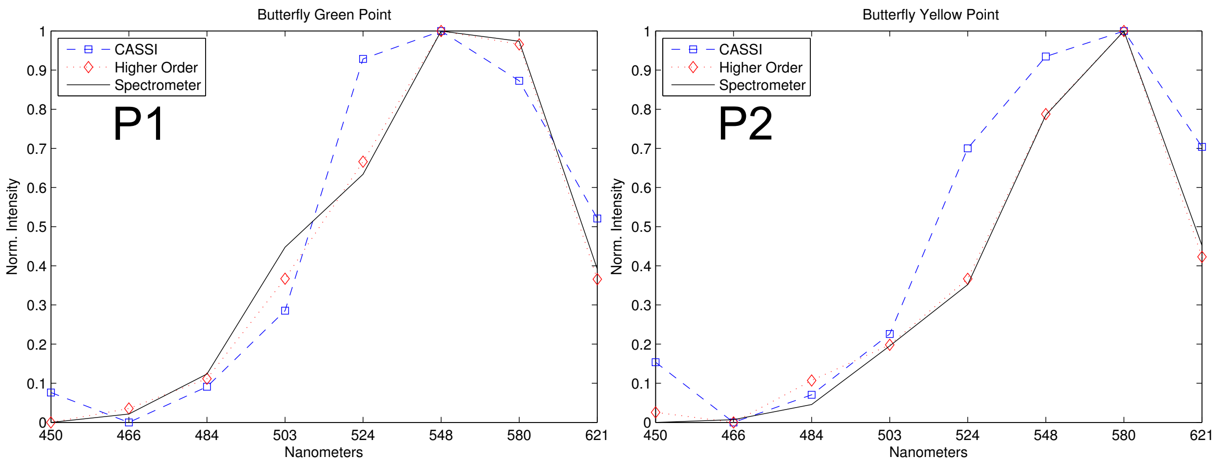

Figure 5.8: Spectral signatures comparison from given points in Fig. 5.7.

taken as the ground truth. The coded apertures as well as the non-linear prism dispersion curve are simulated, and the weights distribution (w_{mnku}) given by Eq. (10) are then synthetically obtained. Noise, as well as blur and misalignment between the coded aperture and the CCD were not added to the model. It can be assumed that this is the ideal case scenario. The latter uses the experimental testbed depicted in Fig. 10(a) to capture the FPA measurement shots. The same fluorescent white illumination source was employed for both cases. However, in the experimental results, the FPA measurements are contaminated by optical aberrations, as well as noise and misalignment between the CCD and the coded aperture. Consequently, the weights distribution (w_{mnku}) presented in Table. 1, is experimentally obtained from the non-linear prism dispersion curve depicted in Fig. 10(b), which is characterized by the use of a monochromatic light source as the input of the testbed ranging between $450nm$ and $650nm$. The reconstruction algorithm utilized (GPSR) is equal for both simulations and experimental results, but differs for each compared model (CASSI vs Higher-Order CASSI). The objects used as targets in the simulation section differs from the ones used in the experimental setup. Due to field of view restrictions in the optical instruments, a set of smaller but spatially richer scenes were selected for the latter.

Chapter 6

CONCLUSIONS

A higher order precision discretization model for coded aperture-based spectral imaging systems has been developed. This model accounts for the inter-voxel projections onto each pixel detector which is disregarded by the first order discretization model. This, in turn, allows for the reconstruction of hyperspectral signals with higher PSNR. Simulations achieve a 4 dB improvement, while testbed experiments visually confirm the simulations results. The proposed model is less-dependent on time-demanding calibration processes, thus leading to multiple-frame CASSI systems to be more suitable for real applications. The results of this work have been recently published in [21].

Future research in this area will focus on hyper-spectral block-processing reconstruction. Firstly, the higher order approach presented in this thesis provides clues on how each voxel is partitioned in subregions and how these are subsequently integrated in the CCD. The knowledge of these small regions can be exploited further to attain a number of advantages. Secondly, block processing allows speed improvements but more important, it can also be exploited for better spatially detailed reconstructions. Higher-order modelling is also expected to improve results in compressive spectral imaging tasks such as classification [22, 23].

BIBLIOGRAPHY

[1] A. A. Wagadarikar, R. John, R. Willett, and D. Brady. Single disperser design for coded aperture snapshot spectral imaging. *Applied Optics*, 47:B44 – B51, 2008.

[2] J. M. Bioucas-Dias, A. Plaza, G. Camps-Valls, P. Scheunders, N.M. Nasrabadi, and J. Chanussot. Hyperspectral remote sensing data analysis and future challenges. *IEEE Magazine on Geoscience and Remote Sensing*, 1(2):6 – 36, 2013.

[3] A. Pelagotti, A. Del Mastio, A. De Rosa, and A. Piva. Multispectral imaging of paintings. *IEEE Signal Processing Magazine*, 25(4):27 – 36, 2008.

[4] R. M. Levenson and J.R. Mansfield. Multispectral imaging in medicine and biology: Slices of life. *Cytometry A*, 69(8):748 – 758, 2006.

[5] R. G. Sellar and G. D. Boreman. Classification of imaging spectrometers for remote sensing applications. *Optical Engineering*, 44(1):013602:1 – 013602:3, 2005.

[6] G. R. Arce, D. J. Brady, L. Carin, H. Arguello, and D. S. Kittle. An introduction to compressive coded aperture spectral imaging. *IEEE Signal Processing Magazine*, 31(1):105 – 115, 2014.

[7] P. Ye, H. Arguello, and G. R. Arce. Spectral aperture code design for multi-shot compressive spectral imaging. In *Biomedical Optics and 3-D Imaging*, page DWA6. Optical Society of America, 2010.

[8] H. Arguello and G. R. Arce. Code aperture design for compressive spectral imaging. 2010.

[9] H. Arguello and G. R. Arce. Rank minimization code aperture design for spectrally selective compressive imaging. *IEEE Transactions on Image Processing*, 22(3):941 – 954, 2013.

[10] H. Arguello and G. R. Arce. Code aperture optimization for spectrally agile compressive imaging. *Journal of the Optical Society of America A*, 28:2400 – 2413, 2011.

[11] H. Arguello and G. R. Arce. Code aperture agile spectral imaging (caasi). In *Imaging and Applied Optics*, page ITuA4. Optical Society of America, 2011.

[12] D. Kittle, K. Choi, A. A. Wagadarikar, and D. J. Brady. Multiframe image estimation for coded aperture snapshot spectral imagers. *Applied Optics*, 49:6824 – 6833, 2010.

[13] Y. Wu, I. O. Mirza, G. R. Arce, and D. W. Prather. Development of a digital-micromirror-device-based multishot snapshot spectral imaging system. *Optics Letters*, 36:2692 – 2694, 2011.

[14] A. A. Wagadarikar, N. P. Pitsianis, X. Sun, and D. J. Brady. Video rate spectral imaging using a coded aperture snapshot spectral imager. *Optics Express*, 17:6368 – 6388, 2009.

[15] E. J. Candes, J. Romberg, and T. Tao. Robust uncertainty principles: exact signal reconstruction from highly incomplete frequency information. *IEEE Transactions on Information Theory*, 52(2):489–509, Feb 2006.

[16] D. L. Donoho. Compressed sensing. *IEEE Transactions on Information Theory*, 52(4):1289–1306, April 2006.

[17] E. J. Candes and T. Tao. Near-optimal signal recovery from random projections: Universal encoding strategies? *IEEE Transactions on Information Theory*, 52(12):5406–5425, Dec 2006.

[18] M. Eismann. *Hyperspectral Remote Sensing*. SPIE Press, 2012.

[19] A. A. Wagadarikar. Compressive spectral and coherence imaging, 2010.

[20] M. Figueiredo, R. Nowak, and S. Wright. Gradient projection for sparse reconstruction: Application to compressed sensing and other inverse problems. *IEEE Journal of Selected Topics in Signal Processing*, 1(4):586 – 597, 2007.

[21] H. Arguello, H. Rueda, Y. Wu, D. W. Prather, and G. R. Arce. Higher-order computational model for coded aperture spectral imaging. *Applied Optics*, 52(10):D12–D21, Apr 2013.

[22] A. Ramirez, H. Arguello, G. R. Arce, and B. M. Sadler. Spectral image classification from optimal coded-aperture compressive measurements. *IEEE Transactions on Geoscience and Remote Sensing*, 52(6):3299 – 3309, 2014.

[23] A. Ramirez, G. R. Arce, and B. Sadler. Coded-aperture compressive spectral image classification. In *Imaging and Applied Optics Technical Papers*, page CM4B.6. Optical Society of America, 2012.

Appendix

DISCLAIMER